EPSC2018

SB12/MD10 abstracts

13 Sep 2018 15:37:32

EPSC Abstracts
Vol. 12, EPSC2018-161-1, 2018
European Planetary Science Congress 2018

Photometric efficiency of a set of geometries

F. Schmidt (1), S. Bourguignon (2)
(1) GEOPS, Univ. Paris-Sud, CNRS, Université Paris-Saclay, Rue du Belvédère, Bât. 504-509, 91405 Orsay, France (2) Laboratoire des Sciences du Numérique de Nantes, École Centrale de Nantes, France (frederic.schmidt@@u-psud.fr)

Abstract

The Hapke model [1] has been widely used to describe the photometric response of a surface (reflectance as a function of incidence and emergence direction). The angular sampling required to constrain the photometric parameters has been widely discussed, but often without strong mathematical basement. A recent study proposed to estimate the uncertainties using a Bayesian approach [2]. We introduce here the concept of "efficiency" of a set of geometries to sample the photometric behavior in the Bayesian framework. A set of angular sampling elements (noted a geometry) is efficient if the retrieved Hapke parameters are close to the expected ones. With numerical simulations, we compared different geometries and found that the principal plane with high incidence is the most efficient geometry among the tested ones. In particular, such geometries are better than poorly sampled full BRDF (Bi-directional Reflectance Distribution Function).

1. Introduction

The Bi-directional Reflectance Distribution Function (BRDF) is the core quantity to describe the photometric behavior [1]. It represents the same location pixel (for picture element), observed with various angular elements (angel, for angular element) [3]. Hapke proposed a semi-analytical model of the BRDF of a granular medium [1]. Many authors have been using it to analyze laboratory data [4, 5], telescopic observations [6], in situ data [7], remote sensing data [8], due to its relative simplicity and fast computation. Following our previous study [2], we do not discuss the realism of the photometric Hapke model, but focus on the data analysis point of view in order to determine the efficiency of a set of geometries to retrieve the Hapke parameters. We will consider here only single scattering albedo (ω), macroscopic roughness (θ), 2-parameter Henyey-Greenstein phase function (b, c). The opposition effects parameters (B_0 and H) are out of the scope of this study since their dependence to small phase angle is obvious.

2. Method

In [2], a Monte-Carlo Markov Chain algorithm is proposed, which generates N_{samp} samples of the parameters of interest. Such samples are (asymptotically) distributed according to the *posterior probability density function,* which merges the likelihood of observed data and possible prior information on the parameter distribution.
In our experiments, we first fix the geometries (incidence and emergence directions). Then, we generate a synthetic observation set with the Hapke model using 12 different combinations (see Table 1). Then, we perform the Bayesian inversion [2] and track how close are the solutions in comparison to the known parameters.

	Configurations
ω (-)	0.1, 0.7
$\bar{\theta}$ (°)	0.5, 25.0
$\{b\,;\,c\}$ (-)	{0.1 ; 1.0}, {0.4 ; 0.4}, {0.8 ; 0.1}

Table 1: Photometric configurations of the Hapke parameters used in the estimation of the efficiency distance E. All 12 combinations of those 4 parameters are tested.

The efficiency distance E is simply computed by considering the proportion of samples that fall inside the correct interval among the N_{samp} samples that were drawn [9]. We then consider that a solution is good if it lies within a 1% error margin (1% smaller and 1% greater than the true value). For each of the 4 parameters, we compute the proportion I and the corresponding distance D=-log(I). The efficiency distance is the sum of all 4 distances for all 4 photometric parameters. Figure 1 shows the relationship between the efficiency distance E and the fraction of good retrieval.

In order to have statistically significant results, we computed the analysis 10 times with random

initialization. Each inversion has been computed with N_{samp}=100,000 samples.

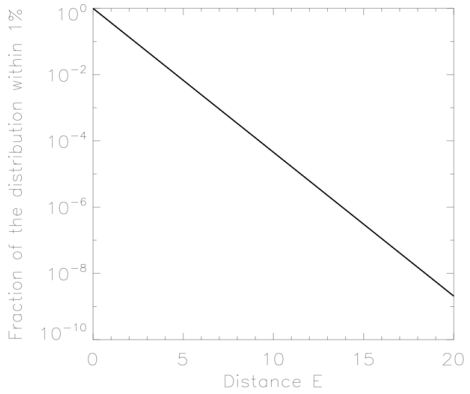

Figure 1: Fraction of the retrieval inside the 1% margin as a function of the efficiency distance E.

3. Results

Table 2 shows the results for several angular configuration. It seems that the 23 geometries proposed by [10] performed as well as a random configuration. Obviously, the worst configuration is the configuration that is perpendicular to the principal plane. Interestingly, the principal plane performs better than the full BRDF.

Table 2: Efficiency distance E for different angular configuration. 23 geometries proposed by [10], 23 geometries taken randomly, 23 geometries perpendicular to the principal plane, 23 geometries in the principal plane (with 75° incidence and up to 82° emergence), 64 BRDF with 40° and 60° incidence and 10-70° emergence.

Geometry	Global efficiency E
23souchon	11.37
23random	10.91
23worst	14.21
23pplane	**8.79**
64brdf	9.26

Figure 2 presents the effect of decimation (removal of intermediate geometries) from the best 23 principal plane configuration. The global efficiency distance E increases as the number of observation directions decreases and E rises significantly more for less than 5 angular configurations.

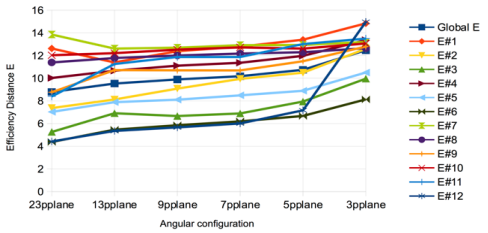

Figure 2: Efficiency distance E as a function of the number of geometry in the principal plane for 12 photometric behavior and the global E. The 23 geometries are decimated but extreme emergence (0° and 82°) are always kept

4. Conclusions

We introduced an index to measure the efficiency of a set of geometries (a collection of directions) to retrieve the proper Hapke parameters. Using the principal plane with high incidence angle seems the best solution with a limited number of directions. In particular, such geometries are better than poorly sampled full BRDF, even with a larger number of directions, due to the too large phase range. We also noticed that 5 directions is the minimum number of angular configurations in the best situation (principal plane) in order to expect well constrained photometric parameters [9].

References

[1] Hapke, B. (1993), Cambridge UP., book [2] Schmidt et al. (2015), Icarus, 260, 73 - 93 [3] Andrieu, F. et al. (2016), The Cryosphere, 2113-2128. [4] Cord, A. et al., (2003), Icarus, 414-427. [5] Johnson, J., (2013), Icarus 383-406. [6] Hapke, Icarus (1998), 89-97. [7] Johnson, J., J. Geophys. Res. (2006), E12S16 [8] Fernando J. et al, (2016), Icarus, 28, 30-51 [9] Schmidt., F. et al. (2018), Icarus, under review [10] Souchon et al., (2011), Icarus, 215, 313-331

EPSC Abstracts
Vol. 12, EPSC2018-222, 2018
European Planetary Science Congress 2018

Dust environment of distant comet C/2014 A4 (SONEAR)

Oleksandra Ivanova (1,2,3), Ludmilla Kolokolova (4), Himadri Sekhar Das (5), Igor Luk'yanyk (3), and Viktor Afanasiev (6)
(1) Astronomical Institute of the SAS, Tatranská Lomnica, Slovak Republic (oivanova@ta3.sk), (2) Main Astronomical Observatory of the NAS of Ukraine, Kyiv, Ukraine, (3) Astronomical observatory, Taras Shevchenko National University of Kyiv, Ukraine, (4) Department of Astronomy, University of Maryland, USA, (5) Department of Physics, Assam University, India, (6) Special Astrophysical Observatory of the RAS, Nizhnij Arkhyz, Russia

Abstract

The results of imaging photometric, polarimetric, and long-slit spectroscopic observations of comet C/2014 A4 (SONEAR) in 2015 are presented. Possible explanation of the unusual polarimetric properties of the dust in this comet is provided.

1. Introduction

Cometary dust preserves the materials left from the early stages of the solar system formation. For those comets that reach close distances to the Sun, the dust does not represent the pristine materials due to sublimation of its volatiles and other changes caused by the solar radiation. However, there are some comets whose orbits keep them far away from the Sun. Some of them exhibit considerable activity at heliocentric distances much larger than 4 au and, thus, allow us to study the dust not notably modified by solar radiation. Since 2011, we are conducting a comprehensive program of polarimetric, photometric, and spectral investigations of active distant comets with the 6-m telescope BTA (SAO RAS).

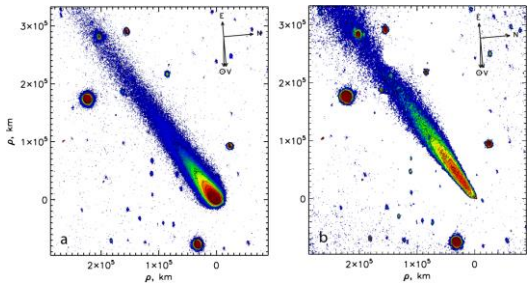

Figure 1: Intensity images of comet A4. The left panel (a) shows the direct images of the comet; the right panel (b) represents processed intensity images emphasizing structure of the coma.

In this work we study one of the distant comet C/2014 A4 (SONEAR), with perihelion distance q= 4.18 AU.

2. Observations

The observations of C/2014 A4 (SONEAR) (hereafter A4) were made with the 6-m telescope BTA SAO RAS on November 5, 2015, when heliocentric (r) and geocentric (Δ) distances of the comet were 4.21 and 3.28 au, and phase angle (α) was 3.8 degree, in both cases. Imaging polarimetric, photometric, and long-slit spectroscopic observations of comet A4 were performed. The observations were taken with a multimode focal reducer SCORPIO-2 of the SAO RAS. A 1024×1024 CCD with a full field of view of 6.1'×6.1' and a pixel scale of 0.18 arcsec/px was used as a detector. Observations were acquired using the broad-band filters.

3. Results

The analysis of spectra and the spatial distribution of intensity, color, and linear polarization over the coma revealed the following features.

3.1 Spectroscopy

No emission lines could be detected. Haser model [1] was used to derive the upper limits to the production rates. We determined upper limits to the emission fluxes of the main neutrals of comets and ion CO^+ and upper limits to the production rates of the molecules CN, C_3, C_2. We also used a polynomial fit to derive the reddening of the spectrum. The polynomial shows linear dependence on wavelengths 21.6 ± 0.2%/1000 Å within the 4650 ÷ 6200 Å wavelength region.

3.2 Image and polarization

The comet showed significant activity with some features in cometary coma and long dust tail at large heliocentric distances. To reveal the low-contrast structures in the cometary coma, we applied the available image enhancement techniques: division by azimuthal average, azimuthal renormalization [2], and rotational gradient method [3]. After processing the image, we revealed bright outflows in the cometary coma. Obtained structures correspond to the dust released from the nucleus, which then moved within the coma as the comet proceeded along its orbit. The dust production was estimated as $Af\rho$=361±1 cm in the r-sdss filter. The polarization images of the comet were taken in the r-sdss (λ6200/600 Å) filter. Polarization map, obtained at the heliocentric distance r = 4.2 au, shows spatial variations of polarization over the coma from about –2% near the nucleus to –5%.. Thus, the negative polarization is significantly greater than the typical polarization (~ 1.5%) observed for the dust of the comets close to the Sun. Based on the computer modeling of the dust as a polydisperse ensemble of multishaped rough spheroids [6], were provided the explanation of the unusual polarimetric properties of the dust in this comet.

4. Summary and Conclusions

The main aim of our observations of distant comets is to study properties of their dust. Most probably dust in distant comets is different than dust in short-period comets, the study of polarization of distant comets is very important for investigation of their physical properties. Photometric and polarimetric observations of distant active comets with specific features (such as long tails, jet structures, and asymmetric comae) are of particular interest. Our photometric and polarimetric observations of dynamically new comet C/ 2014 A4 (SONEAR) showed a considerable level of activity (extended dust coma and tail) at heliocentric distances of 4 au. Since molecular emissions were not detected in the spectra of this comet, it allowed us to study reflective dust properties without gas emission effect. It is known that the shape of the cometary coma as well as the distribution of the coma brightness tells us about the cometary activity, but detailed mechanisms of the activity of comets at large heliocentric distances are not well understood. Polarization map of comet A4 show spatial variations of the polarization. The obtained values of the degree of polarization are significantly higher in absolute values (of polarization over the coma from about –2% near the nucleus to –5%) than the typical value of polarization (~1.5%) observed for the whole coma of most comets closet to the Sun. Our modelling shows that the specifics of the dust in the distant comet A4 is presence of significant amount of ice and organics which likely sublimate at the smaller heliocentric distances.

Acknowledgements

The observations at the 6-m BTA telescope were performed with the financial support of the Ministry of Education and Science of the Russian Federation (agreement No. 14.619.21.0004, project ID RFMEFI61914X0004). OI is supported, in part, by the project 16BF023-02 of the Taras Shevchenko National University of Kyiv, the SASPRO Programme, REA grant agreement No. 609427, and the Slovak Academy of Sciences (grant Vega 2/32/14).

References

[1] Haser, L.: Distribution d'intensite dans la tete d'une cometes, Bull. Soc. R. Sci. Liege, Vol. 43, pp. 740–750, 1957.

[2] Samarasinha, N.H., Larson, S.M.: Image enhancement techniques for quantitative investigations of morphological features in cometary comae: a comparative study, Icarus Vol. 239, pp. 168–185, 2014.

[3] Larson, S., Sekanina, Z.: Coma morphology and dust-emission pattern of periodic comet Halley. I - High-resolution images taken at mount Wilson in 1910, Astron. J. Vol.89, pp. 571–578, 1984.

[4] Tozzi, G. P., Cimatti, A., di Serego Alighieri, S., Cellino, A.: Imaging polarimetry of comet C/1996 B2 (Hyakutake) at the perigee, Planet. Space Sci., Vol. 45, pp. 535–540, 1997.

[5] Farnham, T.: Radial surface brightness profiles as diagnostic tools in cometary dust comae, Bull. Am. Astron. Soc., Vol. 40, pp. 412, 2008.

[6] Kolokolova, L., Das, H.S., Dubovik, O., Lapyonok, T. and Yang, P., 2015. Polarization of cosmic dust simulated with the rough spheroid model. Planetary and Space Science, 116, pp.30-38.

EPSC Abstracts
Vol. 12, EPSC2018-273, 2018
European Planetary Science Congress 2018

MOVIS catalog: near-infrared colors and taxonomy of asteroids observed by VISTA-VHS survey

M. Popescu(1,2,3), J. Licandro(1,2), J. de León(1,2), D. Morate(1,2) , I.L. Boacă(3)

(1) Instituto de Astrofísica de Canarias (IAC), C/Vía Láctea s/n, 38205 La Laguna, Tenerife, Spain (mpopescu@imcce.fr); (2)Departamento de Astrofísica, Universidad de La Laguna, 38206 La Laguna, Tenerife, Spain; (3) Astronomical Institute of the Romanian Academy, 5 Cuțitul de Argint, 040557 Bucharest, Romania;

Abstract

We present the updated version of the MOVIS-C catalog based on VISTA-VHS DR5 release. The near-infrared colors - (Y-J), (H-Ks), (J-Ks) are provided for 53 447 Solar System objects, thus being the largest set of spectro-photometric data in the near-infrared region. Taxonomic classification based on a probablistic approach and machine-learning methods is provided for 9,097 asteroids included in this catalog.

1. Introduction

Spectro-photometric data in the near-infrared region provide the means to characterize the surface composition of Solar System objects. A large set of asteroid colors [1] in this wavelength region was obtained based on the VISTA-VHS (VISTA Hemisphere Survey) data. This survey used the Y, J, H, and Ks broad band filters which are centered at 1.021, 1.254, 1.646, and 2.149 microns and a 1.65 deg. field of view mosaic camera [2]. It imaged the entire southern sky hemisphere, about ~19000 square degrees. The observations were performed between November 4, 2009 and October 1, 2017. The last public data release, VHSDR5 (VHSv20161007), contains 141132 logs of stack-frames.

The taxonomic classification of asteroids imaged by these large surveys provides the opportunity to obtain large scale distribution for asteroidal population, to study the faint objects and to select targets for detailed spectral investigations.

We provide a description of the updated version of the MOVIS-C catalog. This includes the taxonomic classification. The color-color plots of the asteroids observed by this survey are compared with the equivalent colors of the meteorites spectra.

2. Methods

In order to recover the small bodies of the Solar System imaged by VISTA-VHS survey a dedicated pipeline was built [1]. This pipeline applied to VHSDR5 provides information for 53,447 Solar System objects, including 57 NEAs (near-Earth asteroids), 431 Mars Crossers, 612 Hungaria asteroids, 51,382 main-belt asteroids, 218 Cybele asteroids, 267 Hilda asteroids, 434 Trojans, and 29 Kuiper Belt objects [3]. Over this sample, there are about 9,097 asteroids having both (Y-J) and (J-Ks) colors measured and magnitude errors bellow $(Y\text{-}J)_{err} < 0.136$ and $(J\text{-}Ks)_{err} < 0.136$. These limits correspond to the second quartile of the errors.

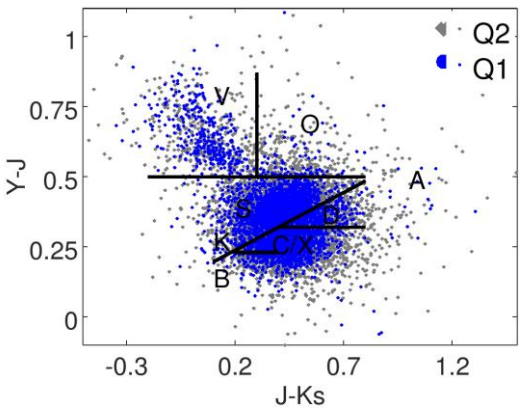

Figure 1: The (Y-J) versus (J-Ks) plot of asteroids reported in the updated version of MOVIS-C catalogue. The Q2 data corresponds to objects with $(Y\text{-}J)_{err} < 0.136$ and $(J\text{-}Ks)_{err} < 0.136$, and the Q1 data to $(Y\text{-}J)_{err} < 0.059$ and $(J\text{-}Ks)_{err} < 0.073$. A diagram corresponding to main taxonomic groups is shown.

A reliable taxonomic classification can be obtained for this sample. This was performed by applying a *probabilistic* approach and *k-nearest neighbor's*

algorithm. The asteroids spectrally classified by [4] were considered as a reference set. Because the information contained by colors provide less constraints than spectral data, the 24 classes were clustered in several groups: B_k^{ni}, C^{ni}, C_{gx}^{ni}, X_t^{ni}, D_s^{ni}, K_l^{ni}, A_d^{ni}, S^{ni}, and V^{ni}. The subscript denotes the interference with other groups.

For asteroid - meteorites comparison, we computed the synthetic colors of meteorites spectral data available in the RELAB database [5].

3. Results

The Solar System Objects found in VISTA-VHS DR5 release are reported in the updated version of the MOVIS-C catalogue. This contains both the NIR colors and the taxonomic classification for objects with (Y-J) and (J-Ks) observed colors [3]. The catalogs are available in electronic form at CDS.

The objects having the errors within the second quartile limits provide a reliable classification for statistical studies. The classification includes 143 bodies classified as B_k^{ni}, 612 as C^{ni}, 199 as C_{gx}^{ni}, 96 as X_t^{ni}, 434 as D_s^{ni}, 531 as K_l^{ni}, 246 as A_d^{ni}, 3303 as S^{ni}, and 807 as V^{ni}. This classification has a ~70% matching with the one provided by Sloan Digital Sky Survey [6].

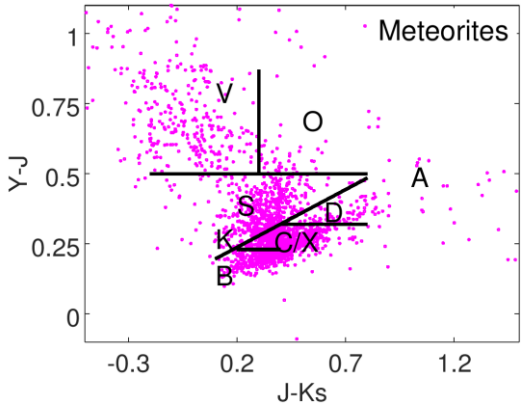

Figure 2: The colors computed from meteorite spectra available in RELAB database. A diagram corresponding to main taxonomic groups derived for asteroid population is overlapped with black color.

The color-color plots of asteroids reported in MOVIS-C catalogue show a broader distribution those computed from meteorite spectra available in the RELAB database. This finding outlines a wider compositional diversity of asteroids not sampled by our current meteorite records.

This large set of data also allows studying the compositional diversity of asteroid families based on their NIR colors [7] and the distribution of basaltic material across the Main Belt [8].

The NIR colors are efficient for identifying end-member classes such as V-types and A-types. By adding the albedo constraint we found that our V-type and A-type candidates have identical size-frequency distributions but a ratio of one to five in favor of V-types. This result adds additional constraints for the hypothesis of "missing mantle problem".

Acknowledgements

This research utilizes spectra acquired with the NASA RELAB facility at Brown University. MP acknowledges support from the AYA2015-67772-R (MINECO, Spain). DM, JL, and JdL acknowledge support from the project AYA2012-39115-C03-03 and ESP2013-47816-C4-2-P (MINECO). The work of ILB was supported by a grant of the Romanian National Authority for Scientific Research - UEFISCDI, project number PN-III-P1-1.2-PCCDI-2017-0371.

References

[1] Popescu, et al. 2016, A&A, 591, A115;

[2] Sutherland, et al. 2015, A&A, 575, A25;

[3] Popescu, et al. 2018, A&A, paper submitted;

[4] DeMeo, F. E., et al. 2009, Icarus, 202, 160;

[5] Pieters, C. M. & Hiroi, T. 2004, LPSC, Vol. 35, ed. S. Mackwell & E. Stansbery;

[6] Carvano, et al. 2010, A&A, 510, A43

[7] Morate, et al. 2018, A&A, forthcoming paper;

[8] Licandro, J., et al. 2017, A&A, 600, A126.

EPSC Abstracts
Vol. 12, EPSC2018-358, 2018
European Planetary Science Congress 2018

Photometric study of Europa with Hapke model

Ines Belgacem (1), Frédéric Schmidt (1) & Grégory Jonniaux (2)
(1) GEOPS, Univ. Paris-Sud, CNRS, University Paris-Saclay, rue du Belvédère, Bat. 504-509 Orsay, France, (2) Airbus Defence & Space, Toulouse, France (contact: ines.belgacem@u-psud.fr)

Abstract

In the context of ESA's future mission JUICE, this work is the start of a broad investigation on the reflectance models of Jupiter's icy moons. It focuses on Europa and Hapke photometric model using images from the LORRI instrument on New Horizons. The parameters are estimated using a Bayesian approach that has been developed for similar work on Mars. We show that it is possible to constrain Hapke parameters on restricted areas of Europa and that they can be fairly different depending on the regions of interest. However, this study shows limitations that we hope to overcome by including more data from other missions such as Voyager.

Introduction

The JUICE (JUpiter ICy moons Explorer) mission from the European Space Agency (ESA) is scheduled to launch in 2022 and arrive at the Jovian system in 2030 to study Jupiter and its icy moons for three and a half years. The spacecraft is being designed by Airbus Defence & Space in Toulouse, France, with a new and innovative navigation system. Any mission to the outer Solar System is challenging considering local radiative and thermal conditions as well as the distance to the Earth. The vision-based navigation algorithm implemented on JUICE will make the spacecraft more autonomous and more precise in its pointing by extracting navigation data from on-board image processing [1]. To offer the best of that algorithm, the spacecraft needs to have a proper knowledge of the photometric models of the moons that will be observed.

Significant work has been done using the Voyager and telescopic observations [2, 3, 4]. But none of these models give satisfying results when simulating images and comparing them to reality. This work aims at studying local photometric properties with the Hapke model [5].

1. Data set

We are using images taken by the LOng Range Reconnaissance Imager (LORRI) on the New Horizons spacecraft. Using [6] we adapted the calibration process to Europa, extracted the measured radiance and converted it to reflectance in REFF units.

$$r = \frac{F_{rad}}{F_{Sun}} \qquad REFF = \pi \frac{r}{cos(inc)}$$

2. Method

2.1 Correction of meta-data

Before anything else, it is essential to correct the images metadata. We have corrected for spacecraft pointing errors as well as moon attitude inaccuracies. To do so, we simulated images using the image renderer developed by Airbus DS, SurRender [7]. Among other things, it allows for custom reflectance model input which is very useful for our study. We used meta-data downloaded on the NASA PDS [8] for the simulations and we compared them to the real images. We then computed the corrections in pointing to make them match using an optimization-based registration function. The attitude of the moon was ultimately refined by computing the optical flow between simulated and real images. The registered movement (fig. 1) was converted to rotation.

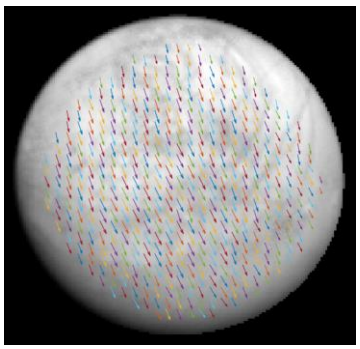

Figure 1: Example of optical flow on image

With accurate meta-data, each pixel was projected onto the moon so the observing geometry – incidence, emission and phase angle – could be computed for all.

2.2 Model and Bayesian Inversion

For this study we are considering Hapke direct model detailed in [5]. Six parameters are to be estimated: b, c, ω, θ, h and B0.

We constrained these parameters in selected areas of Europa using a Bayesian approach that has been used on Mars in the past [9]. No a priori knowledge of the parameters were inferred except for their physical domain of variation. A Monte Carlo Markov Chain algorithm was used to sample the Probability Density Function (PDF) of the a-posteriori solution [9, 10]. The sampling algorithm has been optimized recently [11].

3. Preliminary results

We conducted this local study on nine different zones of interest. Results are rather homogeneous for ω but show some variation for parameters b, c and θ. Fig. 2 shows the distribution for the latter. Since we don't have any data with phase angles lower than 20°, it is impossible to draw any relevant conclusion for h and B0.

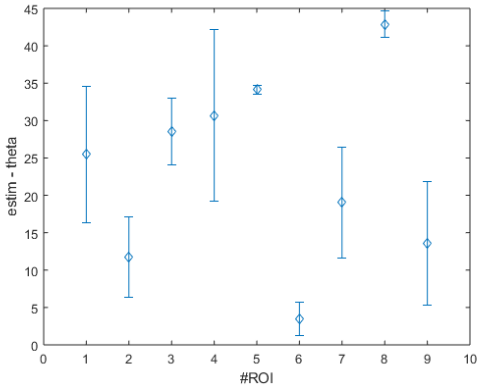

Figure 2: Variation of θ over the different regions of interest

Conclusion

This study shows that we can constrain Hapke parameters on restricted areas of Europa. Thus, local photometric studies should be determined on this moon after additional work. However, we noted that we would need more data to gain confidence in these results and extend the study.

We are working to add data from the Voyager spacecrafts as well as any relevant images from the Cassini and Galileo missions. Because these datasets are very different, each brings its own set of challenges, but we are confident this should help us constrain the photometric properties of Europa and, ultimately, those of Ganymede and Callisto. We will also investigate other photometric models and compare their best fit to fulfill our objective of deriving accurate reflectance models for all three icy moons.

Acknowledgements

This work is supported by Airbus Defence & Space, Toulouse (France) as well as "IDI 2016" project funded by the IDEX Paris-Saclay, ANR-11-IDEX-0003-02.

References

[1] G. Jonniaux and D. Gherardi (2014), Robust Extraction of Navigation Data From Images For Planetary Approach and Landing, 9th ESA GN&CS conference.

[2] B. J. Buratti and J. Veverka, Voyager Photometry of Europa, Icarus, 1983.

[3] D. Domingue and B. Hapke Disk-Resolved Photometric Analysis of European Terrains, Icarus, 1992.

[4] B. J. Buratti, Photometry and Surface Structure of the Icy Galilean Satellites Journal of Geophysical Research, 1995.

[5] B. Hapke, Theory of reflectance and emittance spectroscopy. Topics in Remote Sensing, Cambridge University Press, 1993

[6] F. Morgan et al. Calibration of the New Horizons Long-Range Reconnaissance Imager, Astrobiology and Planetary Missions, 2005.

[7] R. Brochard and N. Despré, SurRender - Image generation software for scientific-level space scene simulation, IPPW 13, 2016.

[8] A.Cheng , NEW HORIZONS Calibrated LORRI JUPITER ENCOUNTER V2.0, NH-J-LORRI-3-JUPITER-V2.0, NASA Planetary Data System, 2014

[9] J. Fernando et al. Surface reflectance of Mars observed by CRISM MRO: 2. Estimation of surface photometric properties in Gusev Crater and Meridiani Planum, Journal of Geophysical Research, 2013.

[10] J. Fernando, F. Schmidt, and S. Douté, Martian Surface Microtexture from Orbital CRISM Multi-Angular Observations: A New Perspective for the Characterization of the Geological Processes Planetary and Space Science, 2016.

[11] F. Schmidt and S. Bourguignon, Efficiency of BRDF sampling and bias on the average photometric behavior Icarus, 2018 (under review)

EPSC Abstracts
Vol. 12, EPSC2018-378, 2018
European Planetary Science Congress 2018

Physical relevance of Independent Component Analysis of planetary radiance

Stéphane Erard

LESIA, Observatoire de Paris, Université PSL, CNRS, Sorbonne Université, Univ. Paris Diderot, Sorbonne Paris Cité, 5 place Jules Janssen, 92195 Meudon, France (stephane.erard@obspm.fr)

Introduction

Independent Component Analysis (ICA) applied to VIRTIS/Venus-Express nightside data [1] allowed us to separate various physical phenomena, based on their spectral signatures in reflected light (1-2.5 µm). Using the complete spectral range (instead of spectral parameters such as band depths) results in extracting complex patterns involving many spectral channels, in particular: O_2 recombination in the high atmosphere on the night side, cloud pattern, limb darkening, and surface emission visible through atmospheric windows.

However, the question of the physical relevance of the independent components retrieved has not been studied in detail, in particular for surface emission. It is here compared with an explicit physical modeling of the spectra performed to map surface temperature and its variations [2].

1. Physical modeling

The VIRTIS/Venus Express dataset was inverted to estimate surface temperature [2]. The flux is measured at 1.02 µm in a narrow window where the atmosphere is not entirely opaque, and is corrected for atmospheric effects. This modeling involves: subtraction of stray light (originating from the illuminated crescent close to the field of view, plus solar reflected light scattered on the night side); correction of limb darkening; correction of multiple reflections between the lower atmosphere and the cloud layer; conversion from radiance to temperature.

Stray light is estimated from residual radiance between the atmospheric windows at short wavelength. Multiple reflections in the atmosphere depend on cloud opacity. It is corrected by dividing out a function of the cloud pattern measured at longer wavelength (1.31 µm). A step-by-step application of this method is provided for session VI0373_01: Fig. 9e in [2] displays the flux from the surface, converted to brightness temperature. Since surface temperature is controlled by atmospheric pressure it essentially reflects surface elevation, with possible departures related to thermal anomalies or changing rock composition. This parameter therefore displays specific patterns when 1) the session covers an area with marked topography contrast and 2) cloud opacity is moderate.

2. Multivariate analysis

The same data where analyzed with Independent Component Analysis (ICA) by [1] so as to entangle several phenomena which may have overlapping spectral signatures. ICA being a linear analysis, all retrieved components consist in linear combinations of flux measured in the various spectral channels. By construction, ICA provides results that are less sensitive to measurement noise, and are more physically relevant than Principal Component Analysis (PCA) [3].

The surface emission in particular is estimated from all the spectral channels that contain a contribution from the surface (~10 channels in the 1.02, 1.1 and 1.18 µm windows), and the atmospheric effects are approximated by subtraction of flux measured at all wavelengths dominated by the cloud pattern. In the case of session VI0373_01, the cloud pattern is mostly estimated from several channels in the 1.29-1.31 μm range (which also includes limb darkening) and in the 1.74 μm peak (although in this session it is saturated in some places).

3. Comparison

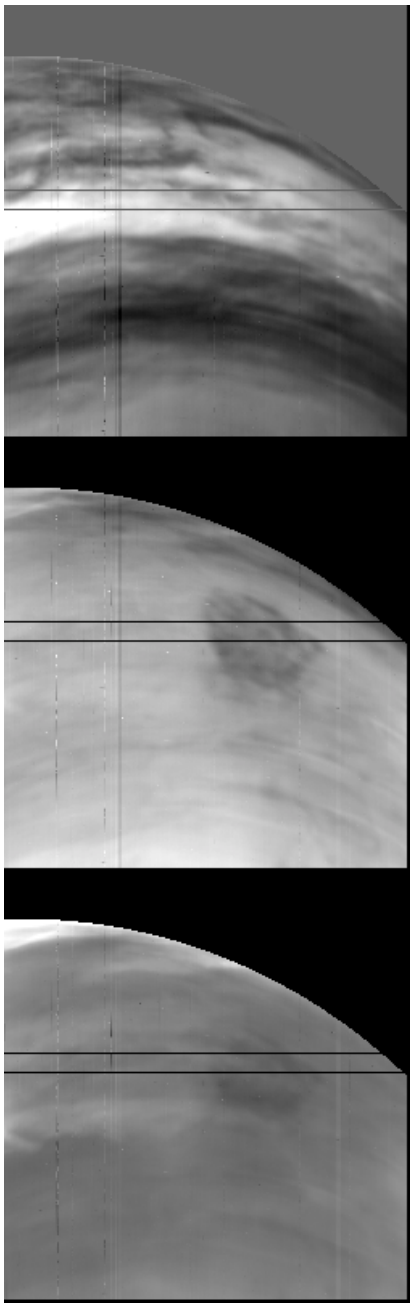

Figure 1: First 3 independent components retrieved on session VI0373_01.

Fig. 1 displays the first 3 components retrieved from the ICA: cloud pattern, surface emission, O_2 emission (from top to bottom). They are essentially decoupled, although a slight mixture between surface and O_2 emission is still apparent. The dark feature on Fig 1b is the high elevation area of Alpha Regio and Eve Corona.

The retrieval of surface emission is at least as good as the one from [2], being less noisy and equally similar to the Magellan altimetry. Both estimates are well correlated except near the limb (Fig. 2). However, the signal is difficult to calibrate in radiance and temperature estimates are biased. Component 1 is also very similar to the cloud pattern estimated in [2], their Fig. 9d. The major differences are low frequency variations along the horizontal direction in [2], now reduced thanks to an improved flat-field.

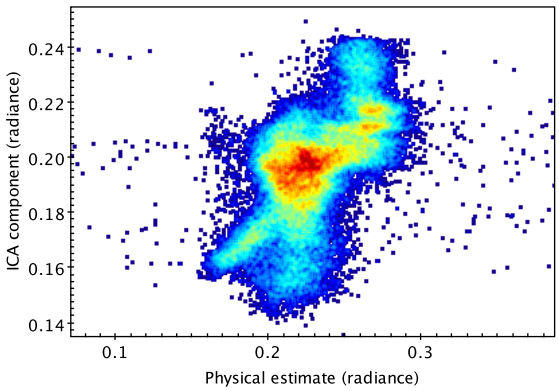

Figure 2: Surface component from ICA compared to physical model on session VI0373_01 (density plot).

This study confirms the ability of ICA to retrieve physical quantities that otherwise require sophisticated modeling, in spite of the linearization performed by ICA.

References

[1] Erard, Drossart and Piccioni (2009) Multivariate analysis of VIRTIS/Venus Express nightside and limb observations. JGR 114(E13), doi:10.1029/2008JE003116.

[2] Mueller et al (2008) Venus surface thermal emission at 1 mum in virtis imaging observations: Evidence for variation of crust and mantle differentiation conditions. JGR 113, doi: 10.1029/2008JE003118.

[3] Erard, S. (2015) ICA applied to imaging spectroscopy remote sensing. EPSC2015–426, Nantes, Fr.

EPSC Abstracts
Vol. 12, EPSC2018-537, 2018
European Planetary Science Congress 2018

Progressive metaheuristics for high-dimensional radiative transfer model inversion

Leila R. Gabasova* (1), Nicolas K. Blanchard (2), Bernard Schmitt (1), Will Grundy (3) and the New Horizons COMP team
E-mail: leila.gabasova@univ-grenoble-alpes.fr
(1) Univ. Grenoble Alpes, CNRS, IPAG, 38000 Grenoble, France, (2) IRIF, Université Paris-Diderot, 75205 Paris Cedex 13, France (3) Lowell Observatory, 1400 W. Mars Hill Rd., Flagstaff, AZ 86001, USA

Abstract

Determining planetary surface composition via remote spectroscopy frequently requires the use of inverse modeling, as the surface presents a complex mixture of materials which cannot be directly identified from the spectra. Depending on the complexity of the radiative transfer model (RTM) used, however, the inverse problem can be nonlinear and very high-dimensional, and the computational cost of traditional optimization methods becomes prohibitive. We demonstrate the utility of a multi-step metaheuristic approach for the inversion of high-dimensional RTMs, using the example of Pluto.

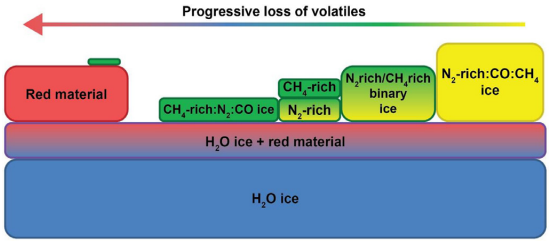

Figure 1: Schematic representation of the various materials present on Pluto and their possible mixing states [1]

1 Example case: Pluto

Since arriving at Pluto in 2015, New Horizons has sent back vast quantities of data, including high-resolution hyperspectral cubes from the LEISA instrument. Data reduction and PCA has allowed us to identify the major types of surface material and to qualitatively map their composition [1]. These types of material interact in multiple ways, including molecular, granular and vertical mixing (Fig. 1). A first quantitative map based on a pixel-by-pixel model inversion has also been created, but the model used is simplified, only taking into account sub-pixel areal mixing [2].

Work is ongoing to produce an accurate surface composition map of Pluto based on the RTM Spectrimag [3], which takes into account a multitude of free physical parameters including grain size, material porosity, and material abundance in the various types of mixtures. As the dimensionality of the model can exceed 40, the search space becomes too big for conventional optimization methods such as gradient descent, and higher-level methods such as metaheuristics may become more efficient.

2 Progressive metaheuristics

When the solution landscape for the inversion problem is "rugged", metaheuristics such as simulated annealing have a strong advantage, as they offer a good compromise between exploration and exploitation. In a high-dimensional landscape, however, randomly drawing initial parameters might not suffice to explore all promising solutions.

To avoid this shortcoming, our proposed method starts by stochastically evaluating the magnitude of effect and variability of each parameter to obtain a ranking. We then use standard metaheuristics to get candidate solutions for a subset of high-importance parameters and progressively increase the dimensionality by including parameters of lesser importance.

We expect this approach to be very fruitful for inverse problems with high-dimensional parametrization in general and the compositional cartography of Pluto in particular, and will discuss the methodology and preliminary results in detail during the congress.

References

[1] Schmitt, B., et al. Physical state and distribution of materials at the surface of Pluto from New Horizons LEISA imaging spectrometer. Icarus 287 (2017): 229-260.

[2] Protopapa, S., et al. Pluto's global surface composition through pixel-by-pixel Hapke modeling of New Horizons Ralph/LEISA data. Icarus 287 (2017): 218-228.

[3] Douté S. and B. Schmitt. A multi-layer bidirectional reflectance model for the analysis of planetary surface hyperspectral images at visible and near infrared wavelengths. J. Geophys. Res. E, 103 (1998): 31367-31390

EPSC Abstracts
Vol. 12, EPSC2018-866, 2018
European Planetary Science Congress 2018

Retrieving the distribution of comet 67P/Churyumov-Gerasimenko surface temperatures for individual Rosetta/VIRTIS-M spectra (pixel) by linear spectral unmixing – Method and first results –

Jean-Philippe Combe (1), Thomas B. McCord (1), Fabrizio Capaccioni (2), Gianrico Filacchione (2), Federico Tosi (2), Mauro Ciarniello (2), Andrea Raponi (2), David Kappel (3), Baptiste Rousseau (4)
(1) Bear Fight Institute, Washington, United States of America, (2) INAF-IAPS, Rome, Italy, (3) DLR, Berlin, Germany, (4) IPAG - Université Grenoble-Alpes, France, (jean-philippe_combe@bearfightinstitute.com)

Please make sure that your pdf conversion results in a document with a page size of 237 x 180 mm!

1. Introduction

Knowledge of surface temperature and its variations as function of illumination conditions is key for understanding the thermodynamical properties, the chemical properties and the physical structure of the regolith (porosity, roughness) of planets and small bodies in the solar system. The surface temperature can be retrieved from near-infrared spectra at wavelengths where thermal emission becomes non-negligible with respect to the reflected components. At 5 µm, the longest wavelength measured by VIRTIS-M [1] on the Rosetta mission [2] which observed comet 67P/Churyumov-Gerasimenko (67P/C-G), the minimum brightness temperature that can be measured is ~150K [3] (instrumental noise equivalent temperature). The usual technique is to fit a Planck function to each spectrum, providing one temperature per pixel (e.g. [3], [4], [5]).
However, the calculation of a distribution of temperatures per pixel is justified by the fact that the local topography changes at all scales resulting in variable illumination conditions (variable incidence angle and shadow casting) within the area covered by each pixel. This causes a distribution of temperatures which turns out in a distribution of thermal emission contributions [6].
Furthermore, the combination of different thermal emission contributions (the linear combination of several Planck curves) is not a Planck function. Consequently, fitting one Planck function to a spectrum results in retrieving a value for the brightness temperature that is not representative of thermophysical properties of the regolith, because it is not the average of all temperatures in the area covered by that pixel.

2. Method: Inversion of multiple Planck curves

Our approach is to perform a linear spectral unmixing of thermal functions, because the spectral thermal emission in each spectrum is the sum of all the thermal contributions that correspond to each facet of the surface, weighted by their areal proportion. We are developing a technique that is based on the Multiple-Endmember Linear Spectral Unmixing model (MELSUM) [7], which has been developed to fit reflectance spectra of particulate surfaces (or laboratory samples) by a linear combination of spectral endmembers (spectra of pure minerals, or spectra collected from relevant locations in the database). With this technique, a spectrum is considered as a vector, and the spectral library of endmembers as a matrix. The inversion relies on the covariance vector and covariance matrix. Its main feature is to be able to test one by one each linear combination of N spectral endmembers among a total of M available in order to retrieve the best one, and to ensure that all spectral endmembers selected contribute positively. Typically, N is 2 to 5, and M is ~10 to 20. This technique has been applied successfully to map the surface composition of Mars [7] with the OMEGA imaging spectrometer on Mars Express, Vesta [8] and Ceres [9] with the VIR mapping spectrometer on the Dawn spacecraft.
In order to retrieve a distribution of temperatures with MELSUM, each spectral endmember is a Planck curve that corresponds to one value of surface temperature. The assumptions in MELSUM are:
- The sum of all weighing coefficient must not exceed 1 (the sum of all illuminated parts within the surface covered by one pixel must not exceed the total surface covered by that pixel).

- The weighing coefficients must not be negative (they can be 0 if the corresponding temperature is absent in the surface observed)
- The temperatures that can be tested are limited by a range and a resolution (typically ≤1 K).
- The maximum number of spectral endmembers (the maximum number of Planck curves) that can be used to fit a spectrum must be small (<5). This is necessary because the total number of combinations to be tested equals M!/(N!×(M-N)!), which increases rapidly as function of N. As a consequence, the number of representative temperature values within a given pixel cannot exceed 5: this is the main limitation of this technique.

3. Results: First evaluation of our inversion model

We have already tested with some success the spectral fitting approach for the retrieval of temperature values and their areal proportions within the area covered by one pixel. 1) We have demonstrated that we can fit the spectra with a sum of Planck curves. 2) MELSUM is a tool that is already functional for processing hyperspectral datasets. 3) Using MELSUM, we have observed that with a model constrained to use a maximum of two or three spectral endmembers (two or three values of temperatures), areas illuminated with a low incidence angle resulted in a selection of only one temperature (or two temperatures separated by the resolution interval of 1K), whereas areas illuminated with a high incidence angle forced the model to select two or three temperatures separated by an interval of several tens of degrees. Our first analysis (Figure 1) indicates that this behavior may be systematic, which is consistent with our expectations: under high incidence angles, a rough surface presents facets that are fully illuminated by the sun, and facets that are shaded (high contrast and variability in the distribution of temperature), whereas under low incidence angle, most facets appear fully illuminated from the point of view of the instrument, near the zenith position.

These preliminary results are encouraging, and they justify pursuing this approach. The obvious area of improvement is computing performance, since it takes several tens of seconds to process a single spectrum executed with the Interactive Data Language (IDL, Harris Geospatial Solutions) on a 64-bit operating system, with a dual core CPU clocked at 2.50 GHz (Intel i5-3210M).

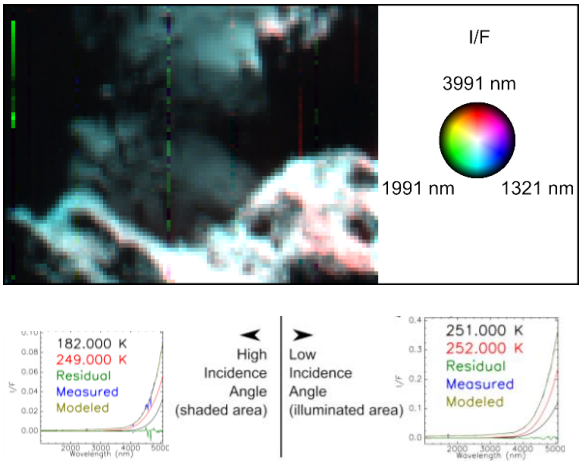

Figure 1: Spectral modeling of thermal emission contributions in Rosetta/VIRTIS-M IR spectra of comet 67P/Churyumov-Gerasimenko using MELSUM with two Planck curves (two surface temperatures) for each pixel. Spectra of shaded areas are systematically modeled by two temperatures separated by several tens of degrees, whereas illuminated areas are always modeled by temperatures separated by one degree.

The current efforts consist in improving the performance and computer efficiency. In addition, each approach can be used to correct the spectra for thermal emission contribution, and thus to map absorption bands that are partially masked or distorted, such as the absorption band at 3.2 µm of organics, or carbonate absorption bands at 4. µm and beyond. These maps could also provide some feedback and could help calibrate the thermal emission correction models.

Acknowledgement

The funding for this research was provided under the ESA Rosetta mission through a subcontract (ROS-1411) from the NASA/Jet Propulsion Laboratory.

References

[1] Coradini A. et al. (2007) *Space Sci. Rev. 128*, 529-559.
[2] Schulz, R. (2009) *So. Sy. Res. 43*.
[3] Tosi, F., et al. (2018). Submitted to Nat. Astron.
[4] Clark R. N. (1981) *JGR 86*, 3074-3086.
[5] Tosi F.. et al. (2014) *Icarus 240*, 37-56.
[6] Bandfield J. (2009) *Icarus 202*, 414-428.
[7] Combe J.-Ph. et al. (2008) *PSS, 56*, 951-975.
[8] Combe J.-Ph. et al. (2015) *Icarus, 259*, 53-71.
[9] Combe J.-Ph. et al. (2018) *Icarus*, in press.

EPSC Abstracts
Vol. 12, EPSC2018-943-3, 2018
European Planetary Science Congress 2018

Corrections of the PFS/MEx perturbations

Alina G. Meresescu (1,2), Matthieu Kowalski (2), Frédéric Schmidt (1)
(1) GEOPS, Univ. Paris-Sud, CNRS, Universite Paris-Saclay, Rue du Belvedere, Bat. 504-509, 91405 Orsay, France, email: alina-georgiana.meresescu@u-psud.fr,
(2) L2S, Univ. Paris-Sud, Supelec, CNRS, Universite Paris-Saclay, 3 rue Joliot Curie, 91192 Gif-sur-Yvette, France

Abstract

The Planetary Fourier Spectrometer (PFS) instrument on board the Mars Express mission generated a large database of spectral information for the Red Planet from the start of its mission. The objective of this work is to correct major limitations of the instrument caused by micro-vibrations which generate "ghosts" in the acquired spectra. The observed spectra can be seen as a convolution between the original clean Martian spectra and perturbation kernels. A blind deconvolution approach in the field of inverse problems is used to remove the ghosts from the measured Martian spectra through an Alternating Minimization algorithm (AM). Constraints are applied so that the estimates respect the physical properties of the investigated signals.

1. Introduction

The ghost problem of the Mars spectra was first analyzed in [4]. In [6] and [5] a precursor methodology of the one proposed here was presented. First, the analytical model was developed to justify the first-order approximation by convolution [6]. There are three sources for Mars spectrum ghosts: the sampling step error and the cyclic misalignment of the cubic corner mirrors of the interferometer, both due to micro-vibrations caused by other instruments on board the mission satellite and the asymmetry error of the interferogram due to the random start of the acquisition. By mathematically modeling these errors and inserting them into the definition of a monochromatic source, we have observed that these errors are represented by Diracs at specific frequencies and have a harmonic propagation behavior inside the Mars spectra. Therefore the kernel must be estimated with a sparsity inducing algorithm that can handle complex values.

Based on that work, a first attempt of blind deconvolution was proposed [5]. Typical results of this strategy are shown in fig. 1. The averaged spectrum shows a pronounced smooth aspect indicating that an algorithm to estimate one Mars spectrum should be able to deliver smooth solutions that additionally are real and positive.

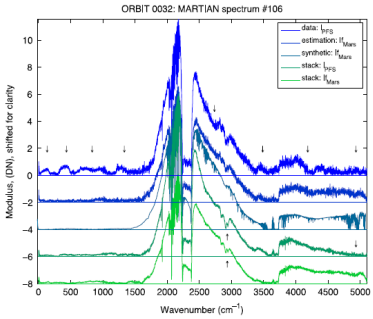

Figure 1: In Figure 1 the first spectrum from above is the measured spectrum from the PFS containing ghosts marked by arrows. The second spectrum is the result from [5] while the third is a synthetic simulation. The last two are an average of 11 non-treated spectra and an average of 11 estimated spectra with [5] respectively.

2. Methodology

2.1. Direct problem

$$m * k = s \tag{1}$$

Where: $\mathbf{s} \in \mathbb{C}$ is the measured spectrum, $\mathbf{k} \in \mathbb{C}$ is the perturbation kernel, $\mathbf{m} \in \mathbb{R}$ is the original Mars spectrum, $*$ is the convolution.

2.2. Inverse problem

$$||s - m * k||_2^2 + \lambda_m ||Dm||_2^2 + \lambda_k ||k||_1 \tag{2}$$

Where: $||s - m * k||_2^2$ is the fidelity to the data term, $\lambda_m ||Dm||_2^2$ is a smoothing regularization term and $\lambda_k ||k||_1$ is a sparsity inducing regularization term. This expression is non-convex but does become convex if one of the regularization terms is fixed.

2.3. AM Algorithm

To estimate **m**, we use an AM algorithm with two alternating steps: to estimate Mars a projected Newton algorithm [2] is used in the first step while the kernel is considered known, then to estimate the kernel a FISTA algorithm [1] is used while the Mars signal is considered known:

Initialize $m_0, k_0, \alpha_{m_0}, J_{old} = 0, \hat{s} = m_0 * k_0$

$J_i = ||s - \hat{s}||_2^2$

While $|J_{old} - J_i| > \epsilon_{stop}$

1. $\Delta_{n_i} = (M_{i-1}^T M_{i-1} + \lambda_{m_i} D^T D)^{-1} \cdot M_{i-1}^T \hat{s}$
   $m_i = P((1 - \alpha_{m_i}) \cdot m_{i-1} + \alpha_{m_i} \cdot \Delta_{n_i})$
   update α_{m_i}, choose best λ_{m_i} from given range
2. $k_i = P\left(\underset{k}{prox}\left(k_{i-1} + \frac{\lambda_{k_i}}{L} m_i^*(s - m_i * k_{i-1})\right)\right)$
   choose best λ_{k_i} from given range
3. check stopping criterion:
   $J_{old} = J_i, \hat{s} = m_i * k_i$
   $J_i = ||s - \hat{s}||_2^2 + \lambda_{m_i} ||Dm_i||_2^2 + \lambda_{k_i} ||k_i||_1$

End While

Where: Δ_{n_i} and α_{m_i} are the Newton's step and step size, J_i is the functional value at each iteration, P is the projection on the constraints given, $prox$ is the proximal of k_i onto a convex subset [3], L is the Lipschitz constant.

3. Results and Conclusions

In Figure 2 the same spectrum from the same orbit as in [5] is presented: the measured spectrum, the result from [5] and the result from our AM algorithm. Mars-AM shows a smoother estimated spectrum, with an attenuation of the ghosts and preservation of the absorption bands. Regarding the AM algorithm itself there are three major improvements: automated choice of λ_m and λ_k hyper-parameters at run time with different strategies, the algorithm allows constraints to be applied on the estimated signals (real valued, positivity) and the addition of an automatic stopping criterion for the estimation. This new strategy opens new perspectives on the correction of the full PFS dataset.

Acknowledgements

This work is supported by the Center for Data Science, funded by the IDEX Paris-Saclay, ANR-11-IDEX-0003-02. We acknowledge support from the "Institut National des Sciences de l'Univers" (INSU), the "Centre National de la Recherche Scientifique" (CNRS) and "Centre National d'Etude Spatiale" (CNES) and through the "Programme National de Planétologie" and MEX/PFS Program.

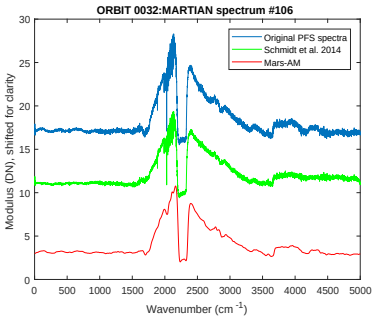

Figure 2: Preliminary results of our new approach. (i) PFS measured spectrum, (ii) Previous results from [5], (iii) Our AM algorithm.

References

[1] A. Beck and M. Teboulle: A Fast Iterative Shrinkage-Thresholding Algorithm for Linear Inverse Problems, SIAM J. Img. Sci., Vol. 2, pp. 183-202, 2009

[2] D.P. Bertsekas: Projected Newton methods for optimization problems with simple constraints, SIAM Journal on control and Optimization, Vol. 20, pp. 221-246, 1982

[3] N. Parikh and S. Boyd: Proximal Algorithms,Found. Trends Optim., Vol. 1, pp. 127-239, 2014

[4] B. Saggin and L. Comolli and V. Formisano: Mechanical disturbances in Fourier spectrometers, Appl. Opt., Vol. 46, pp. 5248-5256, 2007.

[5] F. Schmidt and I. Shatalina and M. Kowalski and N. Gac and B. Saggin and M. Giuranna: Toward a numerical deshaker for PFS, Planetary and Space Science, Vol. 91, pp. 45-51, 2014.

[6] I. Shatalina and F. Schmidt and B. Saggin and N. Gac and M. Kowalski and M. Giuranna: Analytical model and spectral correction of vibration effects on Fourier Transform Spectrometer, SPIE, 2013.

EPSC Abstracts
Vol. 12, EPSC2018-952, 2018
European Planetary Science Congress 2018

Stray light in Rosetta/VIRTIS-H

François Andrieu (1), Stéphane Érard (1) and Dominique Bockelée-Morvan (1)
(1) LESIA, Observatoire de Paris, PSL Research University, CNRS, Sorbonne Universités, UPMC Univ. Paris 6, Univ. Paris Diderot, Sorbonne Paris Cité, France (francois.andrieu@obspm.fr)

Abstract

Evidences have been found that the VIRTIS-H spectrometer's signal can be contaminated with stray light in particular geometric conditions. The variability of this stray light with time and geometry was investigated. It is now possible to model the stray light for a given observation, in order to remove it from the signal.

1.Introduction

The Rosetta spacecraft was sent in 2004 and reached its main target comet 67P Churyumov-Gerasimenko in 2014. One of its main objectives was to study the cometary nucleus and to determine its main characteristics. To do this, the probe had a battery of instruments, including the cross-dispersion spectrometer VIRTIS-H [1]. This type of instrument allows, by first dispersing the light in the high orders by two networks, then separating these orders of diffraction by a prism, to simultaneously acquire the entire spectrum on a matrix of detectors, and this at high spectral resolution. VIRTIS-H has a 1300-3000 resolution in the range 1.88-5.03 µm.

2.Stray light in spectra

Figure 1 shows how stray light contaminate the data. It is clear on Figure 1 that stray light is not dispersed as it is present also outside the area where signal is expected (the bright lines that correspond to orders of diffusion). In this case of backup mode data, the complete image on the detector has been conserved, but most of the time, in nominal mode, only the pixel where signal is expected are saved, to save bandwidth. This means that stray light contamination cannot be measured separately from the real signal. Figure 2 shows how stray light affects a measure: in this example, the spectrum correspond to an observation of the black sky, where no signal is expected. The spectrum displayed is then an artifact only due to stray light contamination.

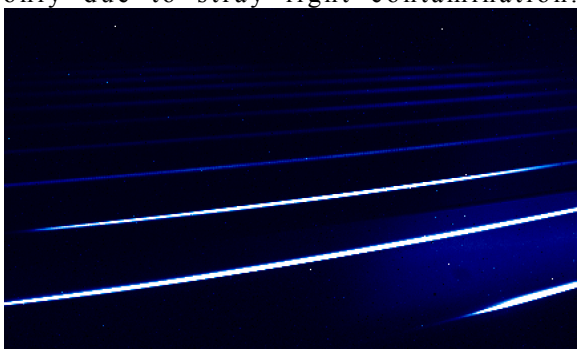

Figure 1: Stray light observed on VIRTIS-H detector in cube H1_00389083498. There should be no signal between the dispersion orders (bright lines)

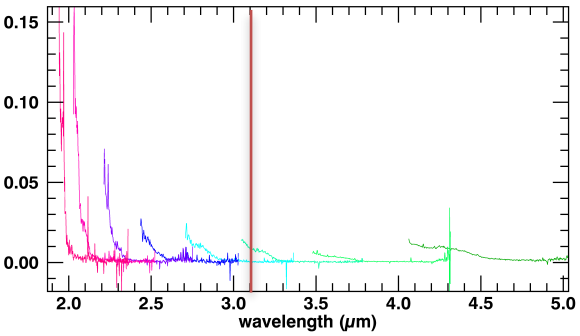

Figure 2: Impact of the stray light on a spectrum: there should be no signal in this example.

3.Variability of stray light

In figure 3 are displayed two images corresponding to the signal at 3.1µm in cube T1_0040235835, but in two different channels in order 2 and 3 (there is an overlap between orders). The red line in Figure 2 shows the locations in a spectrum: in order 3 (image on the left, the 3.1µm channel is never affected by stray light. On the other hand, in order 2, the 3.1µm channel can be contaminated with stray light. When there is no stray light, both channel show the same

signal, but when there is stray light, order 2 displays an higher value than order 3. The geometrical region where stray light is contaminating the data is outline in light red in Figure 3 (right).

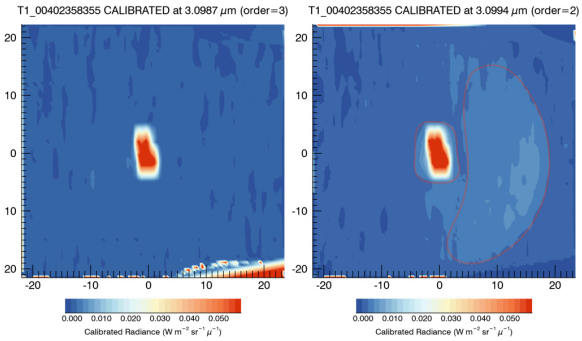

Figure 3: Variability of the stray light with geometry in cube T1_00402358355. Both images show the signal at 3.1µm, but on different orders. Only the canal on the figure on the right is affected by stray light (outlined in light red)

5.Stray light removal

The stray light can be removed from the signal by modeling it and then subtracting its contribution to the original data. As there is a strong variability of the stray light contamination with geometry, different models corresponding to different geometrical condition have been built. They are then scaled using an indicator of stray light in the data, to model empirically the stray light in any observation.

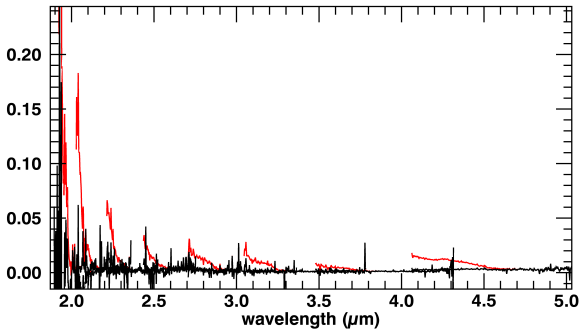

Figure 4: Example of stray light removal: the red curve is the original contaminated data, and the black one is after removal

Figure 4 shows and example of stray light removal in a nominal cube (T1_00396861799). The red spectrum is the original contaminated data, and the black is the corrected spectrum. At first order, the stray light has been removed.

6.Summary and Conclusions

Stray light contaminate a large amount of VIRTIS-H spectral data. It is possible to remove it at first order from the polluted data, by modeling it in different geometrical conditions, scaling it and then subtracting the scaled model to the original data.

Acknowledgements

The authors would like to thank the following institutions and agencies, which supported this work and the development of the VIRTIS instrument: Italian Space Agency (ASI-Italy), Centre National d' Etudes Spatiales (CNES, France), Deutsches Zentrum für Luft und Raumfahrt (DLR, Germany).

References

[1] Coradini, A. et al., VIRTIS: An Imaging Spectrometer for the Rosetta Mission, Space Science Reviews, 2007, 128, 529-559.

EPSC Abstracts
Vol. 12, EPSC2018-974, 2018
European Planetary Science Congress 2018

Analysis of spectral indices for fast mineralogical interpretation of Bennu reflectance spectra

A. Praet (1,2), B.E. Clark (2) M.A. Barucci (1)
(1) Observatoire de Paris, Meudon, France ; (2) Department of Physics, Ithaca College, Ithaca, New York, USA ;
(alice.praet@obspm.fr)

Abstract

The OSIRIS-REx Visible-Infrared Spectrometer will map the surface of asteroid 101955 Bennu from 0.4 to 4.34 μm. The spectrometer is sensitive to a large number of minerals that have features in this wavelength range. In this study, we analyze the efficiency of detection software with spectra of pure minerals with the goal of providing guidance for **fast** spectral map analysis and confidence in mineral detection during operations at Bennu.

1. Introduction

NASA's Asteroid Sample Return Mission OSIRIS-REx (**O**rigins, **S**pectral **I**nterpretation, **R**esource **I**dentification, and **S**ecurity **R**egolith **Ex**plorer) was launched in September 2016, and reaches its target late in 2018. The mission will map and study the Near-Earth asteroid 101955 Bennu and select two possible sampling sites. If there is mineralogical variation across the surface of Bennu, then one region will have a higher science value than another region [1]. We are focused on developing fast mineralogical mapping with data from the OSIRIS-REx Visible-Infrared Spectrometer (OVIRS) [2]. For quick analysis, spectral index (SPINDEX) calculation software has been developed, and is now part of an automated data processing pipeline. For each spectrum of Bennu, SPINDEX calculates 103 spectral indices (absorption band depths and regional continuum slopes). The goal of this study is to calibrate each index with pure mineral spectra in order to select the best spectral indices for mapping Bennu. The mission requires a map of all minerals showing band depth of 5% or more.

2. Data Analysis

Initially, our focus is on oxides (chromite and magnetite) and sulfates (epsomite). Pure mineral reflectance spectra are gathered from the RELAB (Reflectance Laboratory) online database (hosted by Brown University) and the PSF (Planetary Spectrophotometer Facilities) database (hosted by the University of Winnipeg). We then wrote software to resample the laboratory spectra to OVIRS spectral resolution and format them for input to SPINDEX. Additional programs were developed to visualize SPINDEX results, and perform careful analysis of absorption band positions. Magnetite is of particular interest as it has been suggested to be present on Bennu [3].

3. Results

For SPINDEX, each spectral index is numbered and associated with a specific mineral. Based on SPINDEX results, we can separate these bands into strong and weak bands, according to depth. For chromite ($FeCr_2O_4$ Bands 15-20), a total of 15 spectra from the RELAB database were analyzed. Band 15 is the strongest but is not specific to chromite. Hence, a positive detection is required for at least one of the other four weak bands (bands 17, 18, 19, or 20). We find that band 18 is too weak to be of any use (its depth is always below the 5% threshold even for pure minerals), hence to detect chromite on Bennu, we must observe both Bands 15 and 20, the next strongest band. One outcome of our analysis is an improvement of the three wavelengths defining band 20. In Figures 1 and 2, we present band 20 strength after continuum removal according to the old definition (Fig. 1) and according to our new proposed definition (Fig. 2). In Figures 1 and 2, the black dashed line symbolizes the 5% threshold and the dotted line is the wavelength center of the band. This is an example of the type of improvements we are making to SPINDEX.

As for magnetite, only one band index exists in SPINDEX: Band 16. Our analysis of 33 pure magnetite spectra enables us to propose a new definition of the band, shown in Table 1, to better

take into account the absorption feature centered at 0.52 μm. With this improvement, 30% of the magnetite spectra showed positive detection at Band 16, as compared to only 12% previously.

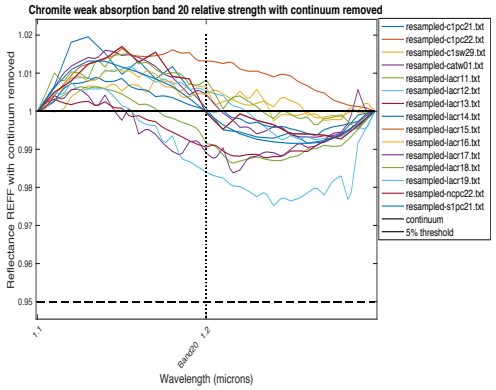

Figure 1: Old definition of Band 20 relative strength with continuum removed.

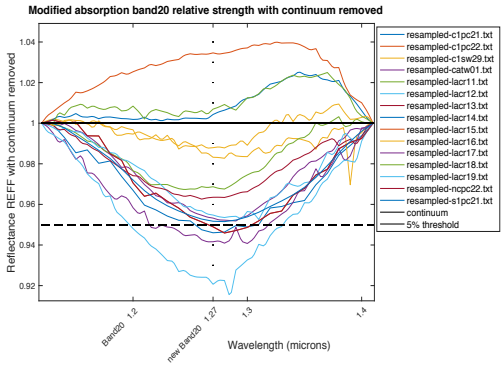

Figure 2: New definition of Band 20 relative strength with continuum removed.

Epsomite is one of the two sulfates detectable with OVIRS (gypsum is the other). Two specific bands (30 and 31) are dedicated to Epsomite. The results of analysis of 6 pure epsomite spectra (from the PSF database) show that both bands can be qualified as strong if we make an improvement to Band 31, shown in Table 1, to better take into account the shape of the absorption feature centered at 1.95 μm. Because it has two strong bands, epsomite, if present on the surface of Bennu, is very likely to be detected.

Table 1: Old and new proposed definition of the SPINDEX bands tested in this study

Band number, and mineral detected	Old definition (left, center and right wavelengths in μm)	New definition (left, center, and right wavelengths in μm)
Band 15 (Chromite)	1.5-2.1-2.7	\
Band 17 (Chromite)	0.55-0.58-0.61	\
Band 18 (Chromite)	0.64-0.67-0.7	\
Band 19 (Chromite)	0.8-0.9-1.0	\
Band 20 (chromite)	1.1-1.2-1.3	1.12-1.27-1.41
Band 16 (Magnetite)	0.45-0.5-0.55	0.41-0.52-0.64
Band 30 (Epsomite)	1.3-1.45-1.75	\
Band 31 (Epsomite)	1.8-1.95-2.25	1.83-1.95-2.25

4. Future Work

In future work, we will analyze SPINDEX results for silicates and hydrated silicates. Ultimately, our work will provide a ranking of the most useful SPINDEX indices in terms of band strength and science value. This will constitute a "Guide to spectral indices" that OSIRIS-REx science team members can use for fast and confident interpretation of OVIRS spectral maps.

Acknowledgements

We would like to thank the astronomers who have shared data and answered our questions during this study: Ed Cloutis and Ellen Howell. A.P. is very grateful to the Physics Department of Ithaca College, researchers and students, and especially to her Master's thesis advisor B.E.C. for all of her helpful advice.

References

[3] Clark et al.: Icarus, Vol. 216, pp. 462-475, 2011. [1] Lauretta et al.: Meteoritics & Planetary Science, Vol. 50, pp. 834-849, 2015. [2] Reuter et al.: Space Science Reviews, Vol. 214, pp. 54-76, 2018.

EPSC Abstracts
Vol. 12, EPSC2018-978, 2018
European Planetary Science Congress 2018

Radiometric Calibration of the Rosetta Navigation Camera

Bernhard Geiger (1), Rafael Andrés (2), Thiago Statella (3) and Maud Barthelemy (2)
(1) Aurora Technology B.V., ESA/ESAC, Camino bajo del Castillo s/n, E-28692 Villanueva de la Cañada, Madrid, Spain
(2) Telespazio Vega, ESA/ESAC, Camino bajo del Castillo s/n, E-28692 Villanueva de la Cañada, Madrid, Spain
(3) Instituto Federal de Educação, Ciência e Tecnologia de Mato Grosso, 95 Zulmira Canavarro, 780025-200, Brazil

Abstract

We have carried out radiometric calibration studies for the Rosetta navigation camera based on images of calibration stars as well as of the extended comet nucleus. In addition, efficient algorithms for artefact correction have been investigated. The results are implemented in a processing pipeline for generating calibrated data products to be delivered to the Planetary Science Archive (PSA).

1. Introduction

During the operational phase of the Rosetta mission images acquired by the navigation camera were processed in near real-time [1] and distributed within the project community. Data sets of uncalibrated images were also made available via ESA's Planetary Science Archive [2, 3].

2. Radiometric Calibration

2.1. Point Sources

Images of stars potentially useful for calibration studies were acquired at a few instances during the cruise phase. Regular images of suitable stars were later scheduled during parts of the comet phase. The measurements indicate no long-term trend of the camera sensitivity. However, the dispersion of data points is large due to a significant dependence of the signal on the intra-pixel position of the point source for the particular CCD type used in the camera.

2.2. Extended Source

Quantitative calibration factors for the navigation camera were determined by means of a cross-calibration analysis with radiometrically corrected OSIRIC-NAC images of the extended comet nucleus [4]. Sets of images acquired with both cameras approximately at the same time and at appropriate nucleus distances were selected for this purpose.

3. Artefact Correction

The following processing steps are applied in order to correct various detector effects and artefacts.

3.1. Bias Field

A bias (and dark) field consisting of a constant offset, gradients in column direction and coherent noise contributions was derived from suitable dark images. The bias field is subtracted from the raw image.

3.2. Smearing

The camera is not equipped with a mechanical shutter. For images with small integration time, the exposure of the CCD during read-out leads to a smearing of the images along the columns. For non-saturated images this artefact can be efficiently corrected by applying appropriate techniques [5].

3.3. Vignetting

An analysis of stacked images showed no evidence for sensitivity variation over the field of view – except for a pronounced vignetting effect in the corners of the CCD. A vignetting field was derived from the available stacked images. An example for the vignetting correction is shown in Figure 1.

3.4. Warm Pixels

For large integration times, an increasing number of pixels show anomalous sensitivity behaviour. A distinctive feature are pairs of adjacent pixels with deviating pixel counts. These effects are corrected by averaging or interpolation based on affected pixel masks.

3.5. Calibration

After applying the correction steps above, the radiometric calibration factors derived from the cross-calibration study are applied to convert the pixel counts into physical radiance units.

3.6. Uncorrected Artefacts

A few types of artefacts such as ghost images, cosmic rays and stray light are difficult to treat in an automated manner and are not considered in the correction procedure.

4. Conclusion

At the time of writing this abstract, the quantitative studies for deriving the calibration factors and auxiliary fields for artefact correction have been finished. The corresponding algorithms have also been implemented in a processing pipeline. However, the masks used for warm pixel and pixel pair correction still need to be further refined. Once this has been achieved, data sets of radiometrically calibrated navigation camera images in PDS format will be generated systematically and provided to the PSA for archiving.

Acknowledgements

Rosetta is an ESA mission with contributions from its member states and NASA. Rosetta's Philae lander is provided by a consortium led by DLR, MPS, CNES and ASI.

References

[1] Geiger, B.: Data processing and visualisation in the Rosetta Science Ground Segment, Acta Astronautica, Vol. 126, pp. 475-487, 2016.

[2] ESA, Planetary Science Archive, User Interface, http://archives.esac.esa.int/psa

[3] ftp://psa.esac.esa.int/pub/mirror/INTERNATIONAL-ROSETTA-MISSION/NAVCAM/

[4] Statella, T., and Geiger, B.: Cross-calibration of the Rosetta Navigation Camera based on images of the 67P comet nucleus, Monthly Notices of the Royal Astronomical Society, Vol. 469, pp. S285-S294, 2017.

[5] Powell, K., Chana, D., Fish, D., and Thompson, C.: Restoration and frequency analysis of CCD images, Applied Optics, Vol. 38, pp. 1343-1347, 1999.

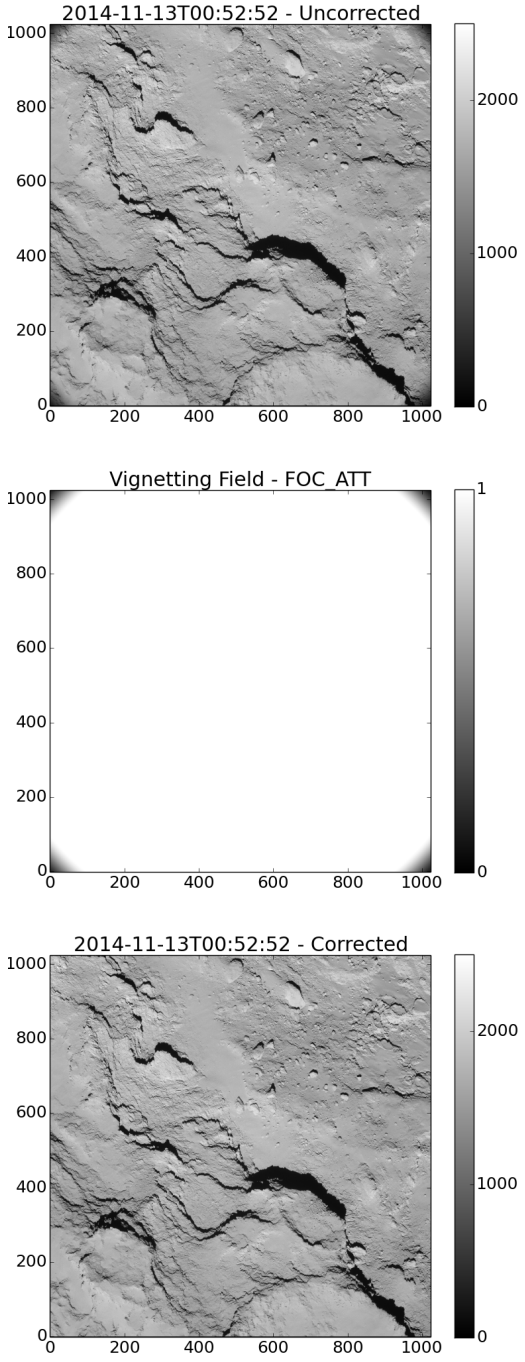

Figure 1: Vignetting correction. Top: Uncorrected image (after bias field subtraction). Middle: Vignetting field generated for artefact correction. Bottom: Corrected image after division by the vignetting field.

EPSC Abstracts
Vol. 12, EPSC2018-1207, 2018
European Planetary Science Congress 2018

Low resolution optical spectra of Jupiter family comets 41P/ and 45P/

Kumar Venkataramani (1,2), Shashikiran Ganesh (1)
(1) Physical Research Laboratory, Ahmedabad, India (kumar@prl.res.in) (2) Indian Institute of Technology, Gandhinagar, India

Abstract

A typical optical spectrum of a comet with well developed coma shows molecular emissions dominated by carbon chain molecules. The Jupiter family comets 41P/Honda–Mrkos–Pajdušáková and 45P/Tuttle–Giacobini–Kresák were spectroscopically observed using the 0.5m telescope at the Mount Abu Infra-red observatory during the period of December 2016 to May 2017. The optical spectra of these comets were obtained using the low resolution spectrograph (LISA) mounted on the telescopes at Mount Abu. As expected in the optical region,the comets exhibited a lot of molecular emission bands including CN,C2,C3,CH and NH2. The spatial profiles of some of these molecules were studied using the traditional theoretical model given by Haser. The low productions rates estimated for these comets indicate an extensive processing of the comet nucleus.

1 Introduction

Comets are cold icy bodies in the solar system that were formed in the solar nebula and are considered to be the signature bodies to understand the formation of the solar system. Cometary molecular emissions are well known and have been studied since a long time. A typical optical spectrum of a comet with well developed coma shows molecular emissions [Kumar et al., 2016] dominated by carbon chain molecules like C_2 and C_3. NH_2 and CN are two other species which show prominent emission lines in the optical spectrum.

These emissions are a result of fluorescing daughter products which are generally produced from photodissociation of the parent species sublimating from the nucleus. Many of the parent species of these products are yet to be confirmed. Results from Rosetta spacecraft have revealed exciting processes that takes place in a cometary nucleus. However, it is vital to observe and study comets in different orbits, to get an overall picture of their formation and evolution. In this work, we have observed and analysed the optical spectra of two Jupiter family comets 41P/ and 45P/.

2 Observations and Reductions

The observations were carried out with LISA spectrograph mounted on the 0.5 m(f/6.8) telescope (PlaneWave Instruments CDK20) at the Mount Abu Infra-red observatory (MIRO), Mount Abu, India. The sky conditions were photometric during the observing period.

Table 1: Observational Log

Comet	Date	Heliocentric Distance r_h (AU)	Solar Phase (degrees)	Exposure (Seconds)
41P/	19/04/2017	1.04	70	400
45P/	09/01/2017	0.56	130	1200

Details of the comet observations are given in table 1. The exposure times mentioned in the table are for each individual frame. A more detailed description of the instrument LISA is given in Kumar et al. [2016]. The slit was placed at the photo-center of the comet and was manually tracked through the guiding CCD throughout the exposure time. The observations were made using the scheme, sky-object-sky, for the proper background sky subtraction.

3 Results and Conclusion

Both the Jupiter family comets exhibited a lot of molecular emissions in their spectra. The optical spectra of the comets are shown in figure 1. The column density profiles for C_2 and CN were obtained for both the comets by integrating the flux at various

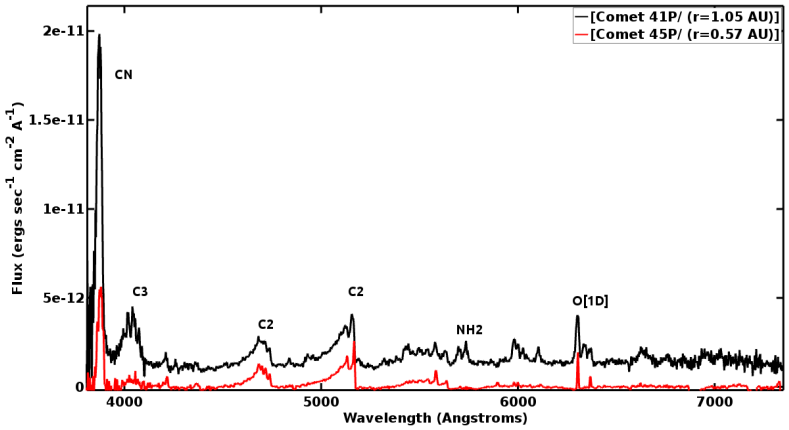

Figure 1: Optical spectra of comets 41P/ and 45P/ obtained from using LISA spectrograph on the 0.5m telescope at the Mount Abu Infra-red observatory, India

. These profiles were then fitted using the standard Haser model. The C2/CN ratio differs significantly in both the comets. This is due to relatively low emissions from CN radical in comet 45P/. Pressuming that HCN is the dominant parent of CN in comets, our results are in accordance with the fact that HCN has been found to be highly deplted in comet 45P/ DiSanti et al. [2017]. The production rates of these molecular species calculated for comet 41P/ turns out to be of the order of about 10^{21} molecules per second.

This is extremely low, as compared to the production rates seen in the Oort cloud comets. This could be due to excessive processing of the volatiles of the Jupiter family comets, due to extremely short orbits and subsequent frequent exposure to high density solar flux impinging the comet surface. Therefore, the low production rates can also be a result of low volatile content in the subsurface of the comet. There have been many instances of outbursts of short period comets [Ishiguro et al., 2016; Pajola et al., 2017]. Although, these molecular emission bands are daughter and grand-daughter products, the behavior of their production rates and scale lengths strongly depends on the parent molecules. The parent molecules originate in the surface layers of the cometary nuclei. They are influenced by many of the orbital parameters like perihelion and aphelion distances and orbital period, inclination, etc. Both of these low inclination Jupiter family comets have close resemblance (in terms of orbital parameters) to the short-period comet 67P/Churyumov–Gerasimenko studied in detail by Rosetta. Therefore, their study gives vital confirmation on the similarity or otherwise of the Jupiter family comets.

Acknowledgements

This work is supported by the Dept. of Space, Govt. of India. We acknowledge the local staff at the Mount Abu Infra-Red Observatory for their help with the observations. We also thank our colleagues in the Astronomy & Astrophysics division at PRL for their comments and suggestions.

References

DiSanti, M. A., Bonev, B. P., Dello Russo, N., et al. 2017, Hypervolatiles in a Jupiter-family Comet: Observations of 45P/Honda-Mrkos-Pajdušáková Using iSHELL at the NASA-IRTF, AJ, 154, 246

Ishiguro, M., Kuroda, D., Hanayama, H., et al. 2016, 2014-2015 Multiple Outbursts of 15P/Finlay, AJ, 152, 169

Kumar, V., Ghetiya, S., Ganesh, S., et al. 2016, Optical spectroscopy of comet C/2014 Q2 (Lovejoy) from the Mount Abu Infrared Observatory, MNRAS, 463, 2137

Pajola, M., Höfner, S., Vincent, J. B., et al. 2017, The pristine interior of comet 67P revealed by the combined Aswan outburst and cliff collapse, Nature Astronomy, 1, 0092

EPSC Abstracts
Vol. 12, EPSC2018-1229, 2018
European Planetary Science Congress 2018

Transient Tracker: An easier way to (photometrically) catch an asteroid or comet.

Pamela L. Gay, Joseph L. Meyers, and The CosmoQuest Team
Astronomical Society of the Pacific (pamela@astrosociety.org)

Abstract

Transient Tracker is open source software designed to identify asteroids and other transient/variable objects in image sets. Transient Tracker's features in final form will include: astrometric and photometric solutions, identification of moving/transient objects, identification of variable objects, and lightcurve analysis. Here we present our first major release candidate and seek community input.

In this release of Transient Tacker, we build on these libraries to add source identification for point / point-like sources, and to do photometry. Our software is released under the Apache 2.0 license on github (github.com/CosmoQuestTeam) and documentation is at cosmoquest.org/TransientTracker.

1. Introduction

Since the earliest days of digital source detection, teams of astronomers and planetary scientists have been trying to devise highly accurate methods for processing images, and extracting and understanding their sources. With a myriad of packages on the market, there is still no truly dominate software solution, but rather, many graduate students and researchers still find themselves writing code from scratch rather than trying to learn how to use difficult freeware like IRAF, or paying for commercial solutions like IDL or MaxIM DL.

With Transient Tracker, we seek to build a solution that may not solve all problems, but will be easily extensible so that it can serve as a foundation for solving many problems. In this presentation, we overview its core features, ease of customization, and how the software can be used to submit results.

2. Planned Features

In creating *Transient Tracker*, we take inspiration from 5 different pieces of software: IRAF, Salsa-J, Astronometry.net, Astrometrica, and VPhot. Each codebase is designed to meet the needs of very different audiences while accomplishing overlapping tasks. From IRAF, we recognize the need to make it easy for scientists to add features, while also learning how not to create an interface. At the other extreme, Salsa-J and Astrometry.net show that students and the public will do science if they have an easy interface that supports all image formats and all computer platforms. Astrometrica and VPhot further demonstrate that people like to be able to export their data so that it can be directly uploaded to archives such as the Minor Planet Center or IAU Central Bureau for Astronomical Telegrams. Taking lessons learned from these code bases, we are working to build an entirely open source platform for data reduction and processing.

Transient Tracker is designed in Java with a codebase that can be added to through Github[1], and an API that easily allows new modules to be added. It will be wrapped for use in a browser, but has the ability to run standalone as well. It will have a two-mode interface; a simple interface that uses default values for settings, and an advanced setup that pairs and easy to use settings tool with rich documentation.

To jumpstart image processing, we built on the NIH hosted ImageJ image processing package [1], which was also used as the basis of SalsaJ. This allows our user community to use TIFF, GIF, JPEG, PNG, DICOM, BMP, PGM and FITS images and provides a broad foundation of image manipulation features to build upon, including the math features needed for dark subtraction, flat fielding, and image stacking. ImageJ already supports the addition of plugins and has rich documentation. Essentially, in the spirit of the open source community, we are forking the ImageJ code base (hosted on NIH servers) and adding to it the features needed for the astronomy and planetary science communities.

[1] https://github.com/CosmoQuestTeam/TransientTracker-PublicRelease

2.1 Image reduction

Transient Tracker provides all the image math routines necessary to process raw data from a telescope. We are building into the existing ImageJ libraries automation to facilitate standardized image processing, as well as support for different kinds of image and pixel rejection.

2.1 Source finding & Photometry

Following the path of the classic software DAOphot, we start off by identifying sources that are a user-entered number of sigma above background (default is 6). With these sources in hand, the images typical FWHM is determined, and aperture photometry can be performed. At this time, Transient Tracker doesn't support PSF fitting, however that may be added via a plugin. Aperture photometry can be used to find relative magnitudes. With additional effort, and either known calibration factors, or images of standard fields, built in routines can be used to transform relative magnitudes into a standard magnitude system.

2.2 Astrometry

With source catalogues in hand, it's possible to match observed stars to standard astrometry catalogues. We will model our approach on Astrometry.net as detailed in Lang et al. (2010) [2]. While our photometry routines will only work on non-loosy data, users will be able to do astrometry (with varying accuracy) on all image types, including compressed files like jpgs. Users will also be able to select moving sources in image sets and output that target's data in the format for reporting to the MPC.

2.3 Additional built in tools

In order to make this software as useful as possible, we are also including basic astronomy tools that are regularly used in image processing and analysis. These include a JD calculator, airmass calculator, and a FITS header reader and editor. These tools are designed to allow users to do everything they need without ever leaving the interface.

3. Software testing

Our goals for our software are: 1) to produce scientifically useful results that have accuracy comparable to IRAF, 2) for our software to be sufficiently easy to use that students can find asteroids as part of a homework assignment, and 3) for it to be easy for researchers to add their own routines to the software.

In order to test our software's accuracy, we will do side-by-side image analysis, comparing our results with IRAF and the SkyX Professional. We expect the results given by all three packages to consistently be within error of one another, with the errors from our software being no greater than those of the two comparison packages.

We will further usability test our software with amateur astronomers, school groups, and university students to verify that it is easy to use and novice users can produce accurate results.

Finally, we will host hack-a-thons at major conferences. This will allow us to see if our target audiences can create and add into the code any additional tools they may want to see. We anticipate holding the first Hack-a-thon in late Q4 of 2018.

Acknowledgements

This project is supported in by NASA grant numbered NNX17AD20A and NNX16AC68A. Any opinions, findings, & conclusions or recommendations expressed are those of this project & do not necessarily reflect the views of the National Aeronautics and Space Administration (NASA). We'd like to thank the Celestron and Oceanside Photo and Telescope for providing us equipment to test our software.

References

[1] Rasband, Wayne, *ImageJ*, http://imagej.nih.gov/ij/docs/index.html

[2] Lang, D., Hogg, D.W., Mierle, K., Blanton, M., & Roweis, S. (2010) *Astrometry.net: Blind astrometric calibration of arbitrary astronomical images.* The Astronomical Journal 139, 1782

.